Hierarchical heterojunctions for enhanced photocatalytic performance and electrocatalytic hydrogen evolution

CHEMISTRY
AN ASIAN JOURNAL

www.chemasianj.org

Accepted Article

Title: Hierarchical MoS2@TiO2 Heterojunctions for Enhanced Photocatalytic Performance and Electrocatalytic Hydrogen Evolution

Authors: Yu Dong, Sheng-You Chen, Yi Lu, Yu-Xuan Xiao, Jie Hu, Si-Ming Wu, Zhao Deng, Ge Tian, Gang-Gang Chang, Jing Li, Silvia Lenaerts, Christoph Janiak, Xiao-Yu Yang, and Bao-Lian Su

To be cited as: *Chem. Asian J.* 10.1002/asia.201800359

Link to VoR: http://dx.doi.org/10.1002/asia.201800359

A Journal of

ACES Asian Chemical Editorial Society

A sister journal of Angewandte Chemie and Chemistry – A European Journal

WILEY-VCH

10.1002/asia.201800359

WILEY-VCH

FULL PAPER

Hierarchical MoS_2@TiO_2 Heterojunctions for Enhanced Photocatalytic Performance and Electrocatalytic Hydrogen Evolution

Yu Dong,[a] Sheng-You Chen,[a] Yi Lu,[a] Yu-Xuan Xiao,[a] Jie Hu,[a] Si-Ming Wu,[a] Zhao Deng,*[a] Ge Tian,*[a] Gang-Gang Chang,[a] Jing Li,[b] Silvia Lenaerts,[c] Christoph Janiak,[d] Xiao-Yu Yang *[a] and Bao-Lian Su [a, e]

Abstract: Hierarchical MoS_2@TiO_2 heterojunctions are synthesized via a one-step hydrothermal method by using protonic titanate nanosheets as the precusor. The TiO_2 nanosheets prevent the aggregation of MoS_2 and promote the carrier transfer efficiency, thus enhancing the photocatalytic and electrocatalytic activity of the nanostructured MoS_2. The obtained MoS_2@TiO_2 significantly enhances photocatalytic activity on degrading rhodamine B (over 5.2 times of pure MoS_2) and acetone (over 2.8 times of pure MoS_2). The MoS_2@TiO_2 is also beneficial for electrocatalytic hydrogen evolution (26 times of pure MoS_2 for cathodic current density). This work offers a promising way to prevent the self-aggregation of MoS_2 and provides a new insight for the design of heterojunctions for materials with lattice mismatch.

Introduction

MoS_2 has become a promising candidate in photocatalysis, energy storage and optoelectronic devices due to its graphite analogous structure and corresponding graphene-like properties.[1-3] However, the great tendency to form irregular aggregation with multi-layered stack greatly reduces the specific surface, blocks the active edge sites, and impedes the carrier transfer.[4] Nanocomposite is an efficient strategy by employing a foreign nanostructure to separate the MoS_2 layers, combine multiple functionalities and form a nano/atomic intimate interface.[5-9] TiO_2 is the most used n-type semiconductor with excellent chemical stability, and has been widely used in MoS_2/TiO_2 p-n heterojunction nanocomposites for enhancing mass/charge transport and structural stability of MoS_2.[10-14] Post-synthesis is often chosen to the rational design, such as TiO_2 nanoparticles doped on MoS_2 thin-layers,[15] MoS_2 nanosheets intersected on/in TiO_2 nanorods,[11] or MoS_2 particles supported in TiO_2 nanoarrays.[16] Notably, it is not easy to obtain the perfect heterojunction growth of MoS_2/TiO_2 structures due to the matching constraints such as lattice constant and atomic arrangement.[7,17] A direct hydrothermal-transformation using nanostructured Ti sources, such as NH_2-MIL-125(Ti) nanocrystals[18] and unilamelled $Ti_{0.87}O_2$ nanosheets,[17] has been recently developed for various heterostructures. The MoS_2/TiO_2 nano-interface fusion[19] in layer-by-layer and core-shell structure not only enhances the photo-electro performance but also provides the MoS_2 with highly structural stability.

Protonic titanate nanosheets (TN) have a very thin nanostructure and thus it is easy to adjust its charge,[20] which could provide nucleation sites for the growth of MoS_2 nanosheets via electrostatic self-assembly. Very interestingly, the layer of TN splitted during the transformation to anatase because of structure change and atoms re-arrange through the hydrothermal process.[21,22] This unique phenomenon would avoid self-aggregation of large-sized layers, and the TiO_2 nanosheets can be uniformly loaded and intimately composite with MoS_2 nanosheets. Moreover, the titanate nanolayer exfoliation from solid-synthesis and osmotic swelling offers an eco-benign and low-cost approach to scale-up the high-performance photo-electro catalysts.[23] Herein, we employ protonic titanate nanosheets as the precursor of TiO_2 nanosheets and use a one-step hydrothermal method to synthesize hierarchical MoS_2@TiO_2 heterojunctions. The TiO_2 nanosheets loaded hierarchically flower-like MoS_2 structure can prevent the aggregation of MoS_2, and enhance the carrier transfer efficiency. The heterostructures exhibit superior performance to pure MoS_2 in the photocatalytic

[a] Y. Dong, S.-Y. Chen, Y. Lu, Y.-X. Xiao, J. Hu, S.-M. Wu, Dr. Z. Deng, Dr. G. Tian, Prof. G.-G. Chang, Prof. X.-Y. Yang, Prof. B.-L. Su
State Key Laboratory Advanced Technology for Materials Synthesis and Processing
Wuhan University of Technology
122, Luoshi Road, Wuhan, 430070, China.
E-mail: dengzhao@whut.edu.cn, tiange@whut.edu.cn, xyyang@whut.edu.cn
[b] Prof. J. Li
The State Key Laboratory of Solid Lubrication, Lanzhou Institute of Chemical Physics
Chinese Academy of Sciences
Lanzhou 730000, China
[c] Prof. S. Lenaerts
Research Group of Sustainable Energy and Air Purification (DuEL), Department of Bioscience Engineering
University of Antwerp
Antwerp, Belgium
[d] Prof. C. Janiak
Institut für Anorganische Chemie und Strukturchemie
Heinrich-Heine-Universität Düsseldorf
40204 Düsseldorf, Germany
[e] Prof. B.-L. Su
Laboratory of Inorganic Materials Chemistry (CMI)
University of Namur
61, rue de Bruxelles, 5000 Namur, Belgium
Supporting information for this article is given via a link at the end of the document.

10.1002/asia.201800359

activity and the electrocatalytic hydrogen evolution, as well as high structural stability.

Results and Discussion

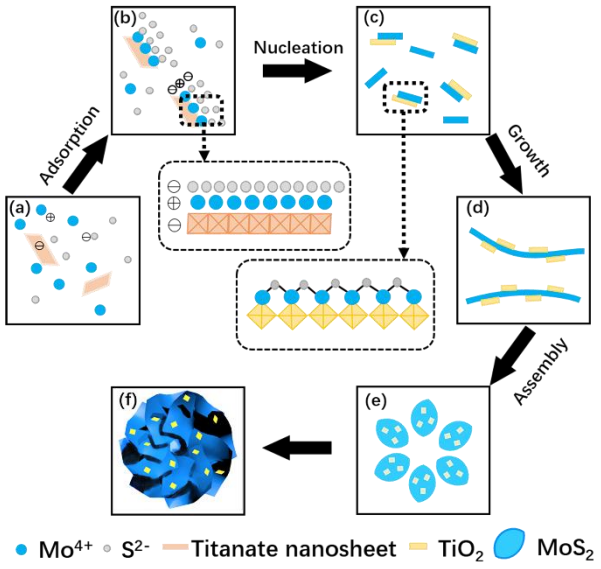

Figure 1. Schematic representation of the formation mechanism of MoS_2@TiO_2: (a) protonic titanate nanosheets (TN) with negatively charged surface in the solution containing Mo source and S source; (b) Mo^{4+} ions are adsorbed on the TN, S^{2-} ions are attracted by Mo^{4+} ions and the electronic-triple-layer form (zoom-in); (c) TN turn to anatase TiO_2 during hydrothermal process, MoS_2 grains nucleate on TiO_2 and form intimate interfaces between MoS_2 and TiO_2 (zoom-in); (d) the growth of MoS_2 nanosheets; (e) self-assembly of MoS_2@TiO_2 layer; (f) the corresponding 3D model.

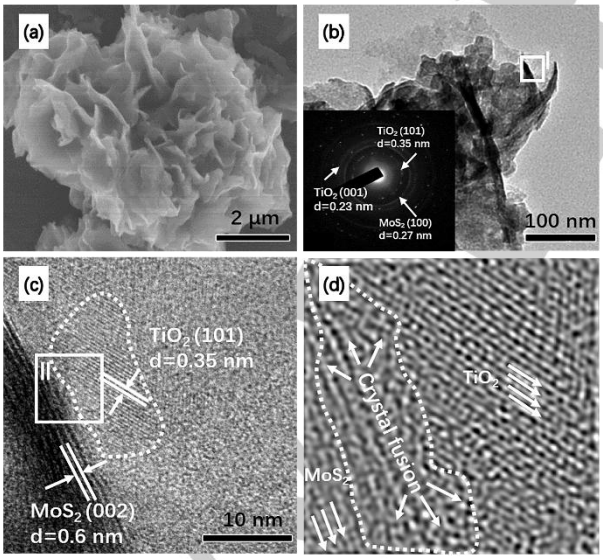

Figure 2. SEM image (a), TEM image (b) and SAED pattern (inset of Figure 2b) of MoS_2@TiO_2 heterojunctions; (c) HR-TEM image of region I; (d) inverse FFT image of region II, showing crystal fusion region between TiO_2 and MoS_2.

Figure 1 presents the synthesis process and formation mechanism of MoS_2@TiO_2. After mixing of the precursors of TN, Mo and S (Figure 1a), the surface adsorption onto protonic titanate nanosheets occurs by electrostatic attraction and negative-positive-negative electric-triple-layers (Figure 1b and zoom-in),[19,24,25] respectively, formed with negative charges caused by the Ti vacancy in the TN, Mo^{4+} ions and S^{2-} ions. During the hydrothermal process, MoS_2 layers nucleate (Figure 1c), grow (Figure 1d) and assemble (Figure 1e). The MoS_2 first tend to nucleate and grow along negative charged TN, and the existence of TN restrain irregular aggregation of MoS_2. MoS_2 grow and form larger sheets, while the TN transform to anatase TiO_2 and split into small-sized nanosheets via the dehydration reaction. Therefore, MoS_2 layers support the TiO_2 nanosheets instead. Typically, with transformation from the TN to TiO_2, the intimate interfaces between MoS_2 and TiO_2 form (Figure 1c and zoom-in). Finally, hierarchically structured MoS_2@TiO_2 heterojunctions (Figure 1e and Figure 1f) are obtained through the self-assembly of MoS_2@TiO_2 nanosheets.

The morphology of MoS_2@TiO_2 heterojunctions is shown in Figure 2. MoS_2@TiO_2 heterojunctions have a hierarchical flower-like structure. In contrast, pure MoS_2 nanosheets tend to aggregate into microspheres (Figure S1), thus blocking the active edge sites. In Figure 2b, it is obvious that MoS_2@TiO_2 is constructed by MoS_2 layers with TiO_2 nanosheets evenly dispersed on the surface of MoS_2, which is consistent with the SAED pattern (inset of Figure 2b). The HR-TEM image shown in Figure 2c presents the heterojunction structure in region I of Figure 2b. The lattice fringes of 0.35 nm agree with the anatase titania (101) interplanar spacing while 0.6 nm fringes correspond to the (002) planes of MoS_2 nanosheets. It is obvious that TiO_2 and MoS_2 are clearly crystalline and form the heterojunction structure. In the corresponding inverse FFT image (Figure 2d taken by region II of Figure 2c) of region II, between TiO_2 and MoS_2, the crystal fusion domain shows a disordered atomic arrangement and strong lattice distortions at the phase edge. This unique fusion structure improves the photoinduced charge carrier transfer and significantly increases the number of catalytically active sites, due to the very low interface losses during electron transmission.[19] This structure formation may be attributed to the nucleation of MoS_2 onto the TN surface based on electrostatic adsorption and atoms re-arrange during hydrothermal process. These nano-fusion domains facilitate the separation of carriers, bond different nanoparticles, and enhance the stability of the nanostructure.[26] Interestingly, compared with protonic titanate nanosheets, TiO_2 nanosheets possess a much smaller size (around 20nm), resulting from the dissolution reaction during the hydrothermal process (Figure S2). The size decrease of TiO_2 nanosheets increases the dispersion of TiO_2, making it uniformly loaded and thus form an intimately composite of MoS_2@TiO_2. To further illustrate the distribution of TiO_2, an EDS analysis is performed in combination with SEM. The element mapping images of Ti, Mo, and S indicate that the TiO_2 uniformly dispersed on MoS_2 (Figure S3).

The structure of MoS_2@TiO_2 is characterized by XRD and N_2 ad-desorption isotherms. The XRD patterns of protonic titanate (HTO), pure MoS_2 nanosheets, MoS_2@TiO_2 and TN after hydrothermal treatment (marked as TiO_2) are shown in Figure S4. As for the pure MoS_2 sample, detected peaks can be assigned to the (002), (100), (101), (102), (103) and (006) planes in the

hexagonal phase (ICDD card no. 37-1492). The diffraction peaks of HTO are as reported before[20]. After exfoliation and hydrothermal treatment of HTO, it turned to anatase TiO_2 (ICDD card no. 21-1272) for the dehydration reaction.[21,22] For MoS_2@TiO_2, the peak at around 25.3° ((101) plane) and 48.1° ((200) plane) are attributed to anatase TiO_2, and the others are consistent with MoS_2. We analyse the surface area via nitrogen-adsorption–desorption isotherms (Figure S5). The specific surface area of MoS_2@TiO_2 is about 3 times that of pure MoS_2. This will promote the exposure of more active sites, increase the contact areas during the reaction, thus improving the photocatalytic activity.[27,28]

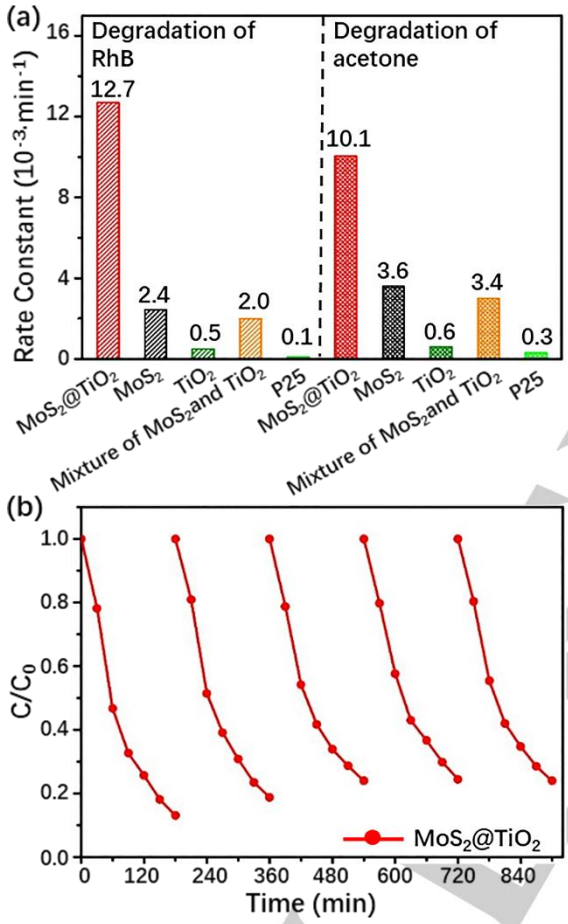

Figure 3. (a) Photocatalytic rate constant of RhB or acetone degradation reaction with MoS_2@TiO_2, MoS_2, mixture of MoS_2 and TiO_2, TiO_2 and P25 under visible-light irradiation; (b) cycle performance of RhB degradation reaction under visible light with MoS_2@TiO_2.

To investigate the photocatalytic properties of the MoS_2@TiO_2, the samples are irradiated under visible light to degrade Rhodamine B (RhB). The comparison of the degradation performance of MoS_2@TiO_2 samples (with the final weight ratio of TiO_2: MoS_2 are 0.02, 0.11, 0.75 from the ICP results (Table S1)) are shown in Figure S6. MoS_2@TiO_2 samples and pure MoS_2 exhibit high adsorption of the dye molecules compared with TiO_2. After visible-light irradiation, the performance is promoted for the heterojunctions and the photocatalytic rate of MoS_2@TiO_2-0.11 is about 5.2 times that of pure MoS_2. Pure TiO_2 and commercial P25 show negligible photocatalytic activity because it cannot absorb visible light (Figure S7). The MoS_2@TiO_2-0.11 shows superior photocatalytic properties and the degradation rate is 2.1 and 3.3 times that of MoS_2@TiO_2-0.02 and MoS_2@TiO_2-0.75, respectively. Small amount load of TiO_2 can hardly prevent the MoS_2 nanosheets from multiple-stacking (Figure S1), while the overloading of TiO_2 would hinder the absorption of visible light. The physically mixed MoS_2 and TiO_2 shows quite lower photocatalytic activity, indicating that the nanofusion interface of MoS_2 and TiO_2 plays an important role in the photocatalytic activity. To probe the durability of the MoS_2@TiO_2 for degradation, we conduct cycle experiments with MoS_2@TiO_2-0.11, and the degradation rate keeps stable after five cycles and retained over 88% (± 2%) of the initial activity (Figure 3b). In the degradation of volatile organic compounds (acetone) (Figure 3a), MoS_2@TiO_2 shows the highest photocatalytic activity and its apparent rate constant (k) reached 10.1×10^{-3} min^{-1}, which is about 2.8 times that of pure MoS_2.

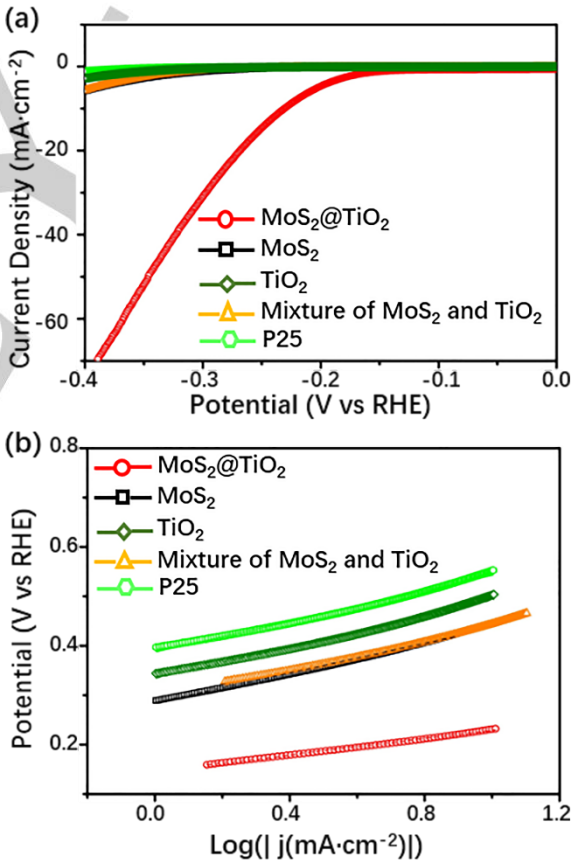

Figure 4. (a) Polarization curves and (b) corresponding Tafel plots of MoS_2@TiO_2, TiO_2, P25, MoS_2, and mixture of MoS_2 and TiO_2.

10.1002/asia.201800359

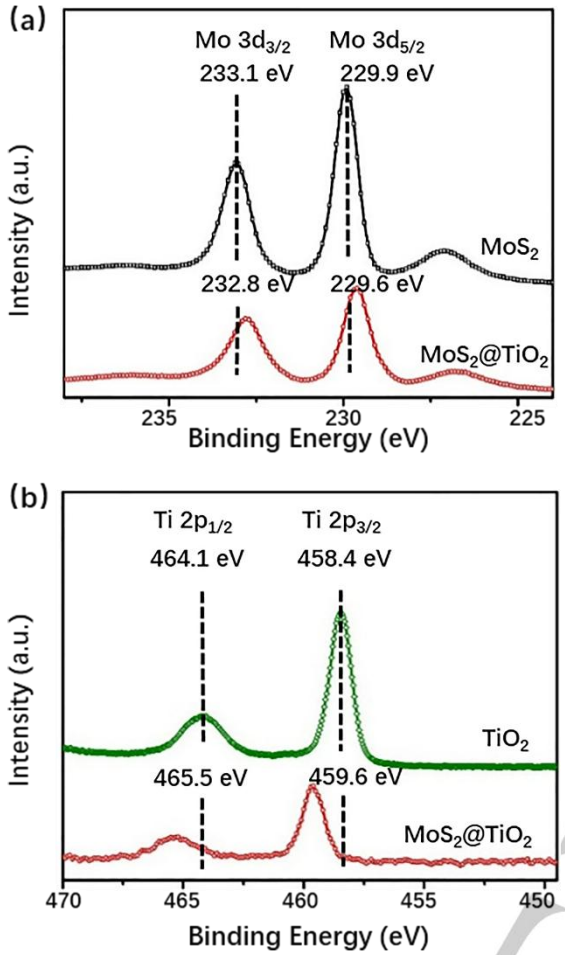

Figure 5. High-resolution XPS curves of (a) Mo 3d and (b) Ti 2p regions for MoS_2, TiO_2 and MoS_2@TiO_2.

Figure 4a and Figure 4b display the electrochemical properties of the samples. TiO_2 exhibits a large onset overpotential of 340 mV for the hydrogen evolution reaction (HER) because of the poor intrinsic conductivity. While for pure MoS_2, the onset overpotential is 230 mV. Our MoS_2@TiO_2 heterojunctions show the decreased onset potential with the value of about 130 mV, which suggests good catalytic activity of the product. Moreover, the MoS_2@TiO_2 heterojunctions display the largest cathodic current density of all the tested samples, with 31.3 $mA{\cdot}cm^{-2}$ at an overpotential of 200 mV, which is about 26 times that of pure MoS_2. Since the cathodic current density is proportional to the quantity of evolved hydrogen, MoS_2@TiO_2 exhibits a prominent hydrogen evolution behavior. In Figure 4b, the Tafel slope of MoS_2@TiO_2 is abot 80 $mV{\cdot}dec^{-1}$, much lower than that of pure MoS_2 (144 $mV{\cdot}dec^{-1}$). The small Tafel slope is advantageous for practical applications, since it will lead to a faster increment of HER rate with increasing overpotential.[29] The Tafel slope comparison confirms that the HER performance of MoS_2@TiO_2 is better than that of the pure MoS_2 and commercial P25. The durability of the of MoS_2@TiO_2 and MoS_2 are tested at static cathodic current (1.96 mA) for 10h. As shown in Figure S8 , the overpotential of MoS_2@TiO_2 only increases 24 mV, while for MoS_2, with the value of 50 mV, indicating MoS_2@TiO_2 are of superior stability in a long-term electrochemical process.

X-ray photoelectron spectroscopy (XPS) is used to investigate the chemical states of Mo, S and Ti in the MoS_2@TiO_2 hetero-structures (Figure 5a, Figure 5b and Figure S9). The high-resolution XPS curves show that the peak at 233.1 eV and 229.9 eV in the pure MoS_2 can be assigned to Mo $3d_{3/2}$, Mo $3d_{5/2}$ respectively in the +4 oxidation state. The binding energy of Mo and S in the MoS_2@TiO_2 both shifted by about 0.3 eV to the lower energy direction. The Ti peaks located at 464.1 eV and 458.4 eV represent Ti $2p_{1/2}$ and Ti $2p_{3/2}$, respectively, indicating the oxidation state of Ti^{4+}. For MoS_2@TiO_2 the Ti $2p_{1/2}$ and Ti $2p_{3/2}$ peaks are shifted to 465.5 eV and 459.6 eV. The shift of peaks indicates possible new bond Ti-O-Mo and the interaction between TiO_2 and MoS_2.[12,30] This result is in good agreement with the TEM observation of Lattice distortion in the actomic-scaled fusion domains, which is also due to the lattice stress and strong interface interaction during the hydrothermal synthesis. This generation of new bond is the direct reason of the change of the chemical enviroment of elements, resulting in the XPS peak shift. The peak at around 530.1 eV in XPS of O 1s (Figure S9b) is ascribed to the formation of the Ti–O–Mo bonds between MoS_2 and TiO_2.[11] Generally, the heterostructure is in favor of the interfacial charge transfer,[31-33] which is the key factor for the photocatalytic efficiency.

Figure 6a shows the periodic on/off photocurrent response of all samples under visible light. After stability pretreatment of 10 cycles (1000 s), the 50th cycle of photocurrent of MoS_2@TiO_2 shows the high stability (83% maintenance of the 10th). On the contrary, other samples exhibit very poor photocurrent response (inset of Figure 6a). It further confirms that the intimate MoS_2@TiO_2 heterojunctions can significantly enhance the photocatalytic activities. The slower decay time implies that photoinduced electrons in the MoS_2@TiO_2 nanocomposite can have much longer carrier lifetime than in MoS_2.[34] Therefore, MoS_2@TiO_2 has better photocatalytic performance than MoS_2 and TiO_2. Moreover, the electron transfer between MoS_2 and TiO_2 is investigated by photoluminescence (PL) (Figure S10). Normally, the PL signals of semiconductor materials result from the recombination of photoinduced charge carriers. The lower PL intensity, the lower recombination rate of photoinduced electron-hole pairs, and the higher photocatalytic activity of semiconductor photocatalysts. The PL intensity of pure MoS_2 and MoS_2@TiO_2 samples reveals a significant decrease with introduction of TiO_2. This indicates that the MoS_2@TiO_2 has a relatively low recombination rate of electrons and holes under visible-light irradiation. This is ascribed to the fact that the electrons are excited from the valence band to the conduction band of MoS_2 and then migrate to TiO_2 nanosheets, which prevents the direct recombination of electrons and holes.

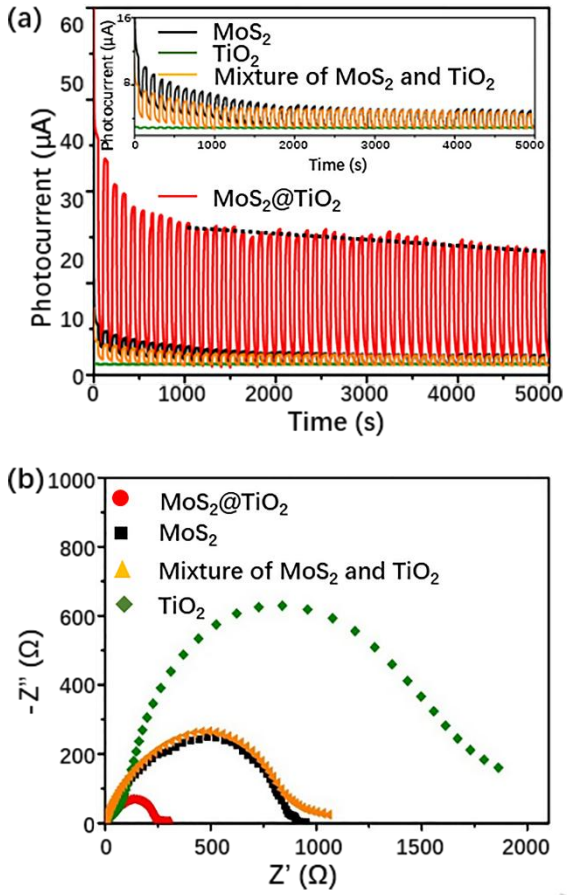

Figure 6. (a) Ttransient photocurrent responses of MoS_2, TiO_2, mixture of MoS_2 and TiO_2 (in set) and MoS_2@TiO_2 in a 0.5 mol/L aqueous Na_2SO_4 solution at 0.5 V bias under visible light irradiation (λ≥420 nm); (b) EIS plot of various samples as indicated for the HER process in a 0.5 mol/L aqueous H_2SO_4 solution.

Furthermore, the electrochemical impedance spectroscopy (EIS) of MoS_2, TiO_2, the mixture of MoS_2 and TiO_2 and MoS_2@TiO_2 is tested at the onset potential (Figure 6b). The charge transfer resistance (R_{ct}) of MoS_2@TiO_2 is 265 Ω, which is much smaller than that of pure MoS_2 (879 Ω). The mixture of MoS_2 and TiO_2 doesn't show enhancement of the charge transfer because of weak interactions between MoS_2 and TiO_2. When TiO_2 and MoS_2 form the heterojunction, the nanofusion interface between TiO_2 and MoS_2 enhances the charge carrier transfer, thus promoting the HER performance.[18,35,36] Also, exchange current densities are obtained via applying extrapolation method to the Tafel plots (Figure S11 and Table S2). As shown in Table S2, MoS_2@TiO_2 exhibits remarkable exchange current density (j_0) of 25.1 μA cm^{-2}, which is about 1.9 times that of pure MoS_2, suggesting the excellent activity for HER catalysis. Since exchange current density is related to electron transfer efficiency, further indicating the enhancement of the charge transfer in our design.

TiO_2 plays two roles for improving electrocatalytic hydrogen reaction evolution performance. Firstly, TiO_2 nanosheets prevent MoS_2 from stacking of the multi-layers and forming of bulk morphology (Figure 2 and Figure S1), which is in favor of the exposure of active sites.[12] The density of active sites can be evaluated by the double-layer capacitance.[37] The calculated double-layer have been used to evaluate the density of active sites[38-41] and show around 13 times that of pure MoS_2 (Figure 12), suggesting the significant increase of the density of active sites. Secondly, the formation of heterojunction between TiO_2 and MoS_2 is beneficial for the efficient electron transport and HER kinetics at the MoS_2@TiO_2 interface (Figure 6b).[18,35]

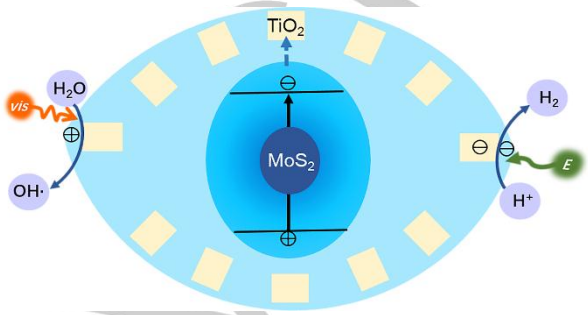

Figure 7. Schematic presentation of the photocatalytic RhB or acetone degradation reaction under visible light (vis) irradiation and HER in MoS_2@TiO_2.

Figure 7 illustrates the proposed mechanism of the photocatalysis and electrocatalysis in MoS_2@TiO_2. The left of Figure 7 depicts the degradation of organic compounds such as acetone and RhB. With the response of MoS_2@TiO_2 under visible light excitation, electrons can migrate from the valence band to the conduction band of MoS_2. Then the photoinduced electrons can be injected from the MoS_2 to the conduction band of TiO_2 because the conduction band of MoS_2 is slightly higher than that of TiO_2 (Figure S13), thus improving the separation efficiency of the photoinduced electron-hole pairs and enhancing the photocatalytic activity. The holes can oxidize water into hydroxyl radicals (·OH) (Figure S14), which are highly oxidative and can react with organic species. The electrocatalytic hydrogen evolution of MoS_2@TiO_2 is illustrated in the right of Figure 7. Similar to the degradation process, electrons can be transfer from the MoS_2 to the TiO_2, facilitating the charge transfer and thus enhancing the electrocatalytic activity.

Conclusions

In summary, hierarchical MoS_2@TiO_2 heterojunctions have been successfully synthesized via a one-step hydrothermal method and exhibit excellent properties in photodegradation and electrocatalytic hydrogen evolution. The enhanced performance may be attributed to two reasons: Firstly, limited aggregation of MoS_2 due to the existence of TiO_2 nanosheets, consequently retaining the exposure of active sites. Secondly, atomic-scaled heterojunctions in MoS_2@TiO_2 is in favor of efficient transfer of charge carriers and thus promoted catalytic activity. This work offers a promising way to prevent the self-aggregation of MoS_2 and provides a new insight for the design of heterojunctions for materials with lattice mismatch.

10.1002/asia.201800359

Experimental Section

Experimental

Cesium carbonate (Cs_2CO_3) (99%), titanium dioxide (TiO_2) (98%), hydrogen chloride (HCl) (37%), ammonium molybdate (VI) tetrahydrate ($(NH_4)_6Mo_7O_{24}\cdot 4H_2O$) (99%) and thiourea ($CH_4N_2S$) (99%) were provided by Sinopharm Chemical Reagent Co., Ltd. Tetrabutylammonium hydroxide ($C_{16}H_{37}NO$) (~25% in H_2O) was provided by Shanghai Aladdin Biochemical Technology Co, Ltd. All chemical reagents were as received without further purification and distilled water was used in the whole experiment

1. Synthesis of Protonic Titanate Nanosheets

Layered cesium titanate $Cs_xTi_{2-x/4}\square_{x/4}O_4$ (CTO) was obtained by solid-state reaction, heating a mixture of Cs_2CO_3 and TiO_2 (5:3 in mole ratio) at 800° C for 20 h. The corresponding protonic form (HTO) was obtained by reacting cesium titanate powder with 1 M HCl aqueous solution at room temperature for 3 days.
During the proton exchange reaction, the HCl solution was replaced with a fresh one every 24 h. The layered protonic titanate was exfoliated into single titanate sheets by intercalating TBA (tetrabutyl ammonium) molecules. In a typical reaction, 0.1g of HTO was added in the mixture of 24.5 mL of deioned water and 0.52 mL of tetrabutylammonium hydroxide, then shaked for 7 days.

2. Synthesis of MoS_2

MoS_2 was synthesized through a simple hydrothermal procedure. 1mmol of ammonium molybdate tetrahydrate and 30mmol thiourea were dissolved in 25 mL of deioned water. The mixture was continued to stir for 30 min before transferred to a 50 mL Teflon-lined autoclave and heated in an air-flow electric oven at 220 °C for 18 h. After cooling to room temperature, the samples were obtained through centrifugal separation, washed with water and ethanol five times and then dried at 60 °C for 12h.

3. Synthesis of MoS_2@TiO_2 Heterojunctions

MoS_2@TiO_2 heterojunctions were synthesized through a simple hydrothermal procedure. In a typical reaction, ammonium molybdate tetrahydrate and thiourea were dissolved in 25mL of 4 mg/mL exfoliated titanate nanosheets suspension. The mixture was continued to stir for 30 min before transferred to a 50 mL Teflon-lined autoclave and heated in an air-flow electric oven at 220 °C for 18 h. After cooling to room temperature, the samples were collected through centrifugal separation, washed with water and ethanol for five times and then dried at 60°C for 12h.
For comparison, 0.09g, 1.0g, 0.11g of $(NH_4)_6Mo_7O_{24}\cdot 4H_2O$ and 16.51g, 1.83g, 0.20g of CH_4N_2S were used respectively to synthesize MoS_2@TiO_2, with the final weight ratio of TiO_2: MoS_2 were about 0.02, 0.11 and 0.75, respectively. The samples were marked as MoS_2@TiO_2-x, x= weight ratio of TiO_2@ MoS_2.

Characterization

The samples morphology observation was performed on a field emission scanning electron microscope (FESEM, S-4800, HITACHI) and a transmission electron microscope (TEM, JEM2100F). Energy-dispersive X-ray spectroscopy (EDS) elemental mapping images were performed in combination with scanning electron microscopy. The power X-ray diffraction (XRD) patterns were recorded on an X-ray diffractometer with Cu Kα radiation (D8 Advance, Bruker, λ = 1.5418 Å). The specific surface area was measured at 77 K by using a Micromeritics ASAP 3020 system. ICP measurements were examined on inductively coupled plasma-atomic emission spectroscopy (ICP-AES, Prodigy7). UV-visible spectra were obtained on a UV-visible spectrophotometer (UV-2550, Shimadzu, Japan). The photoluminescence spectra (PL) were recorded on LS 55 (PERKIN-ELMER) with an excitation wavelength of 500 nm. X-ray photoelectron spectroscopy (XPS) measurements were performed on a PHI Quantera II, (ULVAC-PHI, Japan) for chemical composition analysis, all binding energies were calibrated to the C1s peak at 284.8 eV.

Photocatalytic Activity Evaluation

The photocatalytic activity of samples was estimated from the degradation of rhodamine B (RhB). In a 100 mL of RhB aqueous solution ($1x10^{-5}$ mol), 0.01 g of catalyst was dispersed in a beaker, and the distance between the solution and the lamp was fixed at 10 cm (the excitation power density was 80 mW cm^{-2}). The suspension was stirred in the dark for 30 min to establish the adsorption/desorption equilibrium between the dye molecules until the concentration of RhB no longer changed. As for the irradiation source, a 300 W xenon lamp (PLS-SXE300, Beijing Trusttech Co., Ltd.) with a 420 nm cut-off filter was used in the experiment. The absorbance of the solution was recorded on a UV–vis absorption photometer (UV-2550, Shimadzu, Japan).
In order to test the vapor-phase catalysis of the samples, we chose acetone as the pollutant to detect the performance of the samples. In a typical experiment, we added 10 mg of photocatalysts and 2 mL of ethanol in a glass reactor, then we sonicated the mixed solution for 30 min to get suspension and dried at 40°C for 12 h. The catalysts were deposited on the bottom of the reactor to form thin films. The reactor was then put into a sealed vessel, and we added 5 μL of acetone to the sealed vessel through injection valve to form an initial concentration of 600 ppm. We kept 30mins to balance the concentration of acetone. As for the irradiation source, a 300 W xenon lamp (PLS-SXE300, Beijing Trusttech Co., Ltd.) with was used in the experiment with a 420 nm cut-off filter was used in the experiment. Every 10 minutes we got 100 μL of gas from the system by using syringe and detected the gas with gas chromatograph (GAS CHROMATOGREPH GC 900C).

Electrochemical Measurements

5 mg of catalyst and 50 μL of 5 wt% Nafion solution were dispersed in 950 μL of isopropanol by at least 30 min sonication to form a homogeneous ink. Then 10 μL of the catalyst ink (containing 50 μg of catalyst) was loaded onto a glassy carbon electrode (loading about 0.255 mg/cm^2). Linear sweep voltammetry (using the CHI 660D electrochemical workstation from Chenhua Instrument) with scan rate of 5 mVs^{-1} was conducted in 0.5 M H_2SO_4 using Ag/AgCl electrode as the reference electrode, a graphite rod as the counter electrode and the glassy carbon electrode as the working electrode. AC impedance measurements were carried out in the same configuration at η = -0.25 V from 10^5 – 0.01 Hz with an AC voltage of 5 mV.

Photocurrent Measurements

5 mg of catalyst and 10 μL of 5 wt% Nafion solution were dispersed in 1 ml of water/ethanol mixed solvent (1:1 v/v) by at least 30 min sonication to form a homogeneous ink. Then drop-casting the above ink (50 μL) onto FTO glass with an area of 1 cm^2. Photocurrent tests were carried out in a conventional three-electrode system using on a CHI 660D electrochemical workstation (Chenhua Instrument, Shanghai, China) with a Pt foil as the counter electrode and a Ag/AgCl reference electrode at a 0.5 V potential bias under a PLS-SXE-300C lamp.

Analysis of Hydroxyl Radicals (·OH).

The formation of hydroxyl radicals (·OH) on the surface of visible light-irradiated MoS_2@TiO_2 can be detected by employing terephthalic acid as a probe molecule. Terephthalic acid can react with ·OH and produce fluorescent hydroxy product, 2-hydroxyterephthalic acid. The PL intensity

at about 425 nm gradually increase with the prolongation of irradiation time, indicating the gradual accumulation of ·OH. [42,43].

In a typical experiment, we added 5 mg catalysts in the aqueous solution of 3 mM terephthalic acid and 10 mM NaOH. The suspension was stirred in the dark for 30 min. As for the irradiation source, a 300 W xenon lamp (PLS-SXE300, Beijing Trusttech Co., Ltd.) with a 420 nm cut-off filter was used in the experiment. After irradiated under visible light every 15 min, the reaction solution was collected to measure the PL intensity at 425 nm excited by 315 nm light.

Acknowledgements

This work is supported by National Key R&D Program of China (2017YFC1103800), PCSIRT (IRT_15R52), NSFC (U1662134, U1663225, 51472190, 51611530672, 51503166, 21706199, 21711530705), ISTCP (2015DFE52870), and HPNSF (2016CFA033, 2017CFB487), SKLPPC (PPC2016007).

Keywords: MoS_2 • TiO_2 • Protonic titanate nanosheets • photodegradation• electrocatalytic hydrogen evolution

[1] D. Voiry, M. Salehi, R. Silva, T. Fujita, M. Chen, T. Asefa, V. B. Shenoy, G. Eda and M. Chhowalla, *Nano. Lett.* **2013**, *13*, 6222-6227.

[2] J. Chen, N. Kuriyama; H.-T. Yuan, H. Takeshita and T. Sakai, *J. Am. Chem. Soc*. **2001**, *123*, 11813-11814.

[3] O. Lopez-Sanchez, D. Lembke, M. Kayci, A. Radenovic and A. Kis, *Nat. Nanotech*. **2013**, *8*, 497-501.

[4] M. Shen, Z. Yan, L. Yang, P. Du, J. Zhang and B. Xiang, *Chem. Commun*. **2014**, *50*, 15447-15449.

[5] F. Meng, J. Li, S. K. Cushing, M. Zhi and N. Wu, *J. Am. Chem. Soc*. **2013**, *135*, 10286-10289.

[6] B. Luo, G. Liu and L. Wang, *Nanoscale* **2016**, *8*, 6904-6920.

[7] B. Chen, Y.-H. Meng, J.-W. Sha, C. Zhong, W.-B. Hu and N.-Q. Zha, *Nanoscale* **2018**, *10*, 34-68.

[8] J. Liu, Y. Li, J. Ke, Z. Wang and H.-N. Xiao, *Catalysts* **2017**, *7*, 30, DOI: 10.3390/catal7010030.

[9] L. Zheng, S. Han, H. Liu, P. Yu and X. Fang, *Small* **2016**, *12*, 1527-1536.

[10] X. Zhu, C. Yang, F. Xiao, J. Wang and X. Su, *New J. Chem*. **2015**, *39*, 683-688.

[11] C. Liu, L. Wang, Y. Tang, S. Luo, Y. Liu, S. Zhang, Y. Zeng and Y. Xu, *Appl. Catal., B*. **2015**, 164, 1-9.

[12] L. Guo, Z. Yang, K. Marcus, Z. Li, B. Luo, L. Zhou, X. Wang, Y. Du and Y. Yang, *Energy Environ. Sci*. **2018**, *11*, 106-114.

[13] H. Fu, K. Yu, H. Li, J. Li, B. Guo, Y. Tan, C. Song and Z. Zhu, *Dalton Trans.* **2015**, *44*, 1664-1672.

[14] J. Wang, B. Wei, L. Xu, H. Gao, W. Sun and J. Che, *Mater. Lett.* **2016**, *179*, 42-46.

[15] W. Ren, W. Zhou, H. Zhang and C. Cheng, *ACS Appl. Mater. Interfaces*. **2017**, 9, 487-495.

[16] C. Meng, Z. Liu, T. Zhang and J. Zhai, *Green Chem*. **2015**, 17, 2764-2768.

[17] R. Dai, A. Zhang, Z. Pan, A. M. Al-Enizi, A. A. Elzatahry, L. Hu and G. Zheng, *Small* **2016**, *12*, 2792-2799.

[18] B. Ma, P. Y. Guan, Q. Y. Li, M. Zhang and S. Q. Zang, *ACS Appl. Mater. Interfaces* **2016**, 8, 26794-26800.

[19] Y. Lu, X. Cheng, G. Tian, H. Zhao, L. He, J. Hu, S.-M. Wu, Y. Dong, G.-G. Chang, S. Lenaerts, S. Siffert, G. Van Tendeloo, Z.-F. Li, L.-L. Xu, X.-Y. Yang and B.-L. Su, *Nano Energy* **2018**, *47*,8-17.

[20] T. Sasaki and M. Watanabe, *J. Am. Chem. Soc*. **1998**, 120, 4682-4689.

[21] P.-H. Wen, Y. Ishikawa; H. Itoh and Q. Feng, *J. Phys. Chem. C* **2009**, *113*, 20275–20280.

[22] P.-H. Wen, H. Itoh, W.-P. Tang and Feng, Q, *Langmuir* **2007**, *23*, 11782-11790.

[23] K. Zhu and G. Hu, J. Supercrit. *Fluids* **2014**, 94, 165-173.

[24] N. Jiang, X.-Y. Yang, G.-L. Ying, L. Shen, J. Liu, W. Geng, L. J. Dai, S. Y. Liu, J. Cao, G. Tian, T. L. Sun, S. P. Li and B.-L. Su, *Chem. Sci.* **2015**, *6*, 486-491.

[25] N. Jiang, X.-Y. Yang, Z. Deng, L. Wang, Z. Y. Hu, G. Tian, G. L. Ying, L. Shen, M. X. Zhang and B.-L. Su, *Small* **2015**, *11*, 2003-2010.

[26] X.-Y. Yang, L.-H. Chen, Y. Li, J. C. Rooke, C. Sanchez and B.-L. Su, *Chem. Soc. Rev.* **2017**, 46, 481-558.

[27] B. Lim, M. Jiang, P. H. Camargo, E. C. Cho, J. Tao, X. Lu, Y. Zhu, Y. Xia, *Science* **2009**, *324*, 1302-1305.

[28] X.-F, Li, T.-X, Fan, H, Zhou, S.-K, Chow, W. Zhang, D, Zhang, Q.-X. Guo, and H. Ogawa, *Adv. Funct. Mater.* **2009**, *19*, 45–56.

[29] J. Xie, J. Zhang, S. Li, F. Grote, X. Zhang, H. Zhang, R. Wang, Y. Lei, B. Pan and Y. Xie, *J. Am. Chem. Soc*. **2013**, 135, 17881-17888.

[30] W. Zhou, Z. Yin, Y. Du, X. Huang, Z. Zeng, Z. Fan, H. Liu, J. Wang and H. Zhang, *Small* **2013**, *9*, 140-147.

[31] Z. Lu, L. Zeng, W. Song, Z. Qin, D. Zeng and C. Xie, *Appl. Catal., B* **2017**, *202*, 489-499.

[32] H. Zhou, L. Ding, T.-X. Fan, J. Ding, D. Zhang, Q.-X. Guo, *Appl. Catal. B* **2014**, *147*, 221-228.

[33] L.-Q. Wu, Li,-H, Hao, B. Pang, G.-F, Wang, Y, Zhang and X.-H Li, *J. Mater. Chem. A* **2017**, *5*, 4629–4637.

[34] H. Han, K. M. Kim, C. W. Lee, C. S. Lee, R. C. Pawar, J. L. Jones, Y. R. Hong, J. H. Ryu, T. Song, S. H. Kang, H. Choi and S. Mhin, Phys. *Chem. Chem. Phys.* **2017**, 19, 28207-28215.

[35] Y. Shen, X. Ren, X. Qi, J. Zhou, Z. Huang and J. Zhong, *J. Electrochem. Soc.* **2016**, *163*, H1087-H1090.

[36] X. Song, G. Chen, L. Guan, H. Zhang and J. Tao, *Appl. Phys. Express* **2016**, *9*, 095801.

[37] A. P. Murthy, J. Theerthagiri, J. Madhavan and K. Murugan, *Phys. Chem. Chem. Phys.* **2017**, *19*, 1988-1998.

[38] L. Ma, Y. Hu, G. Zhu, R. Chen, T. Chen, H. Lu, Y. Wang, J. Liang, H. Liu, C. Yan, Z. Tie, Z. Jin and J. Liu, *Chem. Mater.* **2016**, *28*, 5733-5742

[39] J. Liang, C. Wang, P. Zhao, Y. Wang, L. Ma, G. Zhu, Y. Hu, Z. Lu, Z. Xu, Y. Ma, T. Chen, Z. Tie, J. Liu and Z. Jin, *ACS Appl. Mater. Interfaces*, **2018**, *10*, 6084-6089.

[40] J. D. Benck, Z. Chen, L. Y. Kuritzky, A. J. Forman and T. F. Jaramillo, *ACS Catalysis*, **2012**, *2*, 1916-1923.

[41] M. A. Lukowski, A. S. Daniel, F. Meng, A. Forticaux, L. Li and S. Jin, *J. Am. Chem. Soc.* **2013**, *135*, 10274-10277.

[42] K. Ishibashi, A, Fujishima, T. Watanabe and K. Hashimoto; *Electrochem. Commun.* **2000**, *2*, 207-210.

[43] J.-G, Yu, W.-G. Wang, B. Cheng and B.-L. Su, *J. Phys. Chem. C* **2009,** *113,* 6743–6750

10.1002/asia.201800359

WILEY-VCH

Entry for the Table of Contents

FULL PAPER

We employ protonic titanate nanosheets as the precursor of TiO_2 nanosheets and use a one-step hydrothermal method to synthesize hierarchical MoS_2@TiO_2 heterojunctions.

The TiO_2 loaded hierarchically follower-like MoS_2 structure can enhance the carriers transfer efficiency for the formation of nanofusion interface beteween TiO_2 and MoS_2.

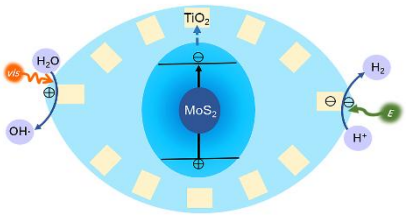

Yu Dong, Sheng-You Chen, Yi Lu, Yu-Xuan Xiao, Jie Hu, Si-Ming Wu, Zhao Deng, Ge Tian,* Gang-Gang Chang, Jing Li,b Silvia Lenaerts,c Christoph Janiak, Xiao-Yu Yang *and Bao-Lian Su*

Page No. – Page No.

Hierarchical MoS_2@TiO_2 Heterojunctions for Enhanced Photocatalytic Performance and Electrocatalytic Hydrogen Evolution